Chemical Science

ROYAL SOCIETY OF CHEMISTRY

EDGE ARTICLE

View Article Online
View Journal | View Issue

Cite this: *Chem. Sci.*, 2025, **16**, 23149

Light-induced access to a fluorescent Cd_7Ag_{21} nanocluster from a halide-supported Cd_8X nanocluster directed by a face-capping macrocyclic metalloligand

Biliu Lan, Ziling Li, Yanfang Feng, Tao Deng, Min Pan and Zhong Zhang *

Received 5th July 2025
Accepted 20th October 2025

DOI: 10.1039/d5sc04963f

rsc.li/chemical-science

Metalloligands with multiple preorganized binding sites provide unique advantages for modulating structural patterns and enhancing the surface stability of metal nanoclusters. However, the precise structure-directing effect of metalloligands in nanocluster transformation remains a missing puzzle piece. Herein, three nested concentric bitetrahedral **Cd_8X** nanoclusters were synthesized through a stepwise evolutionary pathway. These nano-sized architectures comprise tetrahedrally arranged tripodal Cd^{II} macrocyclic metalloligands encapsulating a halide-supported Cd_4 tetrahedron, and the template effect of halide ions on the stabilization of **Cd_8X** was dependent on their ionic size. Initiated by Ag^I, the released metalloligands from **Cd_8Cl** precisely direct the light-activated fabrication of a yellow-emissive $8e^-$ superatomic **Cd_7Ag_{21}** nanocluster. Evidently, different carboxylate O-donor triads and tetrads from the metalloligands geometrically adaptively cap the surface Ag_3 triangles of the convex polyhedral kernel in **Cd_7Ag_{21}**, thus shaping and protecting the multi-silver kernel in the post-transformed nanocluster. Due to the labile coordination between the carboxylate-rich metalloligand and surface atoms of the Ag_{20} kernel, the selective fluorescence quenching response of **Cd_7Ag_{21}** towards cysteine (Cys) can be rationalized by a ligand replacement-cluster aggregation process. This study demonstrates the distinctive utility of the preformed tripodal metalloligand as a passivating agent, facilitating shape- and size-matching with the surface motifs of metal nanoclusters to induce structural transformation, thereby enabling the synthesis of novel nanocluster architectures.

Introduction

As the key nexus between discrete silver atoms and silver nanoparticles (Ag NPs), atomically precise silver nanoclusters (Ag NCs) smaller than sub-3 nm exhibit discontinuous energy levels and molecular-like physicochemical properties. They (Ag NCs) have recently attracted considerable attention in the field of metal nanomaterials owing to extensive applications in optical devices, bio-imaging and catalysis.[1–11] Based on soft-hard acid–base theory, some typical soft-base ligands, including thiolates, phosphines and alkynyls, have been intentionally selected as the stabilizer of soft-acid silver atoms in a general bottom-up route to Ag NCs.[12–21] As the hard–soft mismatch between N/O donors and silver atoms makes it more challenging to stabilize Ag NCs using ligands containing only hard N/O donors, only a handful of groundbreaking studies in recent years have successfully prepared Ag NCs from hard-base ligands, including all-nitrogen-donor ligands, carboxylates and inorganic polyoxometalates.[22–29] With respect to simple N/O-donor ligands, preorganized metalloligands with multiple uncoordinated N/O donors impart higher stabilization and stronger structure-directing control for the growth of Ag NCs.[30–32] For instance, by using the trifurcate TiL_3 metalloligands as capping vertices, the Zhang group constructed a family of progressively larger Ag–Ti NCs where TiL_3 units induce a tetrahedral geometry to the obtained NCs.[33] The Sun group reported that some thiacalix[4]arene-modified polyoxometalates integrate dual functionalities as passivating ligands and anion templates to create Ag NCs with complicated geometric architectures.[34] Nevertheless, a broader exploration is needed for expanding the list of N/O-based metalloligands with enhanced robustness and structure-directing effect for the assembly of Ag NCs.

The ligand- or metal-exchange-induced structural transformation has been found to be a reliable post-synthesis tactic to acquire new metal NCs with some structural features inherited from the precursor NCs. Usually, the presence of these foreign species causes the transformation products to retain the original core size, but it may occasionally lead to the formation

---

School of Chemistry and Pharmaceutical Sciences, Key Laboratory for Chemistry and Molecular Engineering of Medicinal Resources (Ministry of Education of China), Guangxi Key Laboratory of Chemistry and Molecular Engineering of Medicinal Resources, Guangxi Normal University, Guilin 541004, PR China. E-mail: zhangzhong@mailbox.gxnu.edu.cn

of new NCs with distinct sizes and structures.[35–43] Hitherto, stimuli-induced structural transformation of metalloligand-stabilized metal NCs has hardly been explored, and the structure-directing and/or size-manipulating effects of metalloligands for the transformation products remain an unexplored territory. Recently, we have successfully achieved the modular assembly of a trigonal-bipyramidal Ni^{II}-organic cage starting from a tripodal Ni^{II}-based macrocyclic metalloligand, whose facial ligating mode resembles that of the aforementioned TiL_3 moiety in Ag NCs. Inspired by this, we can consider whether this type of metalloligand is competent as a structure-directing and stabilizing agent to achieve the Ag^I-triggered conversion of the metalloligand-based nanocluster precursor to heterometallic Ag NCs.[33,44]

In this work, common halide ions except F^- can serve as a central template to assist the formation of a series of **Cd_8X** (X = Cl^-, Br^- and I^-) NCs, where each triangular face of the central halide-supported Cd_4 tetrahedron is capped by a $[Cd(tacntp)]^-$ metalloligand. Time-resolved ESI-MS analysis explicitly mapped out a stepwise evolution from the mononuclear Cd^{II} metalloligand to the intact cluster skeleton of a **Cd_8I** NC. Competitive binding together with halide substitution assays mutually confirmed that the templating effect of halide ions is enhanced with an increase in the ion size. Owing to the moderate stability of **Cd_8Cl** in CH_3OH, Ag^I drives its disassembly to liberate the Cd^{II} metalloligand, which integrates multiple functions of Ag^I immobilization, kernel shaping and surface passivation to exercise a determining impact on the light-induced production of a yellow-emissive **Cd_7Ag_{21}** NC. Extraneous Cys can substitute for surface-anchored metalloligands of **Cd_7Ag_{21}** followed by the formation of non-luminous Ag NPs. Therefore, the selective recognition of Cys can be achieved *via* a fluorescence switch-off response.

Results and discussion

Three halide-supported **Cd_8X** NCs were obtained as colorless block-like crystals by slowly evaporating an acidic aqueous solution containing $Cd(NO_3)_2\cdot 4H_2O$, 1,4,7-triazacyclononane-1,4,7-tripropionic acid ($tacntpH_3$), and the corresponding potassium halide (KCl, KBr, KI) in a molar ratio of 4 : 2 : 1 for one week. The detailed preparation procedures are included in the SI. However, the attempts to acquire an octanuclear Cd^{II} NC containing an interstitial F^- ion failed when KF was used as a halide source.

The structural elucidation revealed that the three **Cd_8X** NCs adopt different counter anions—OH^- in **Cd_8Cl** and $CdX_4^{\ 2-}$ in both **Cd_8Br** and **Cd_8I**—but share the same Cd_8 cationic skeleton except its entrapped halide ion (Fig. 1a and S1). The crystallographic data and structure refinement parameters for these NCs are listed in Table S1, and the selected bond lengths and angles are included in Table S2. The structural details of the cationic skeleton are presented with **Cd_8Cl** as a representative, where the central Cl_1 atom in the cationic moiety is tetrahedrally bonded to four Cd^{II} atoms (denoted as Cd_i) to generate an inner Cd_4 tetrahedron (Cd_4^{inner}) (Fig. 1b and S2). Benefiting from the pre-organized state of the $[Cd(tacntp)]^-$ metalloligand with hydrophobic macrocyclic backbone and hydrophilic carboxylate groups residing at the opposite sides of the encapsulated Cd^{II} center, each triangular face of Cd_4^{inner} is facially capped by the three uncoordinated carbonyl groups of a metalloligand to afford a tetracapped tetrahedron. Especially, four Cd^{II} atoms in the metalloligands (denoted as Cd_o) constitute an outer Cd_4 tetrahedron (Cd_4^{outer}), which is also centered by the Cl_1 atom. Therefore, the cationic motif may be described as a nested concentric bitetrahedron with a radius of 7.719 Å (Fig. S3). Either of two crystallographically inequivalent Cd_o atoms presents a distorted octahedral geometry completed by three N donors from the backbone of $tacntp^{3-}$ and three O atoms provided by different carboxylate side arms, while each Cd_i atom in Cd_4^{inner} is hepta-coordinated to six carboxylate O atoms stemming from three distinct metalloligands along with the central Cl atom, achieving a highly distorted pentagonal bipyramidal configuration (Fig. 1c and d). The Cd⋯Cd edge lengths of Cd_4^{inner} range between 4.382(6) and 4.546(7) Å, and the distances between Cd_o and Cd_i atoms connected by a bridging-chelating carboxylate group are 4.070(6)–4.209(7) Å. The Cd_i–Cl distances (2.733(10) and 2.742(10) Å) are much

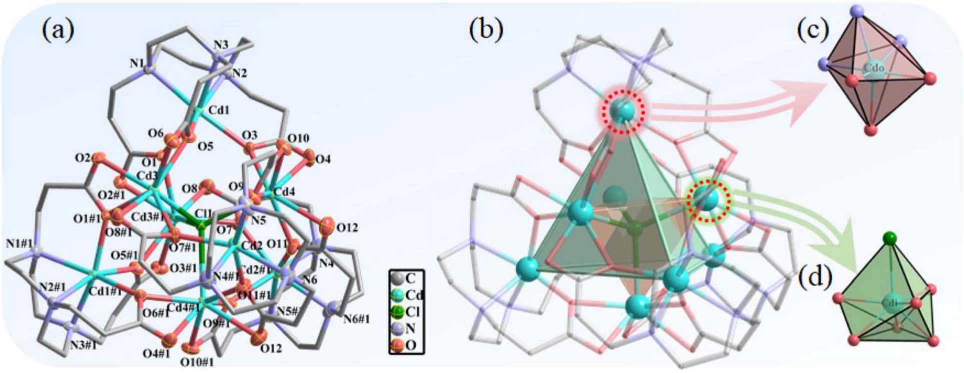

Fig. 1 (a) Structural details of the cationic skeleton of **Cd_8Cl** (30% probability ellipsoids). Symmetry code: #1 $-x+1, -y+1/2, z$. Hydrogen atoms are omitted for clarity. (b) The nested concentric bitetrahedral arrangement of Cd^{II} atoms in **Cd_8Cl**, with Cd_4^{outer} shown in green and Cd_4^{inner} shown in light orange. (c and d) The coordination polyhedra of Cd_o and Cd_i.

shorter than the sum of the van der Waals radii for Cd and Cl atoms of 3.42 Å, signifying the strong binding between Cd^{II} and Cl^-. Compared to **Cd_8Cl**, with increasing size of the templating halide ion, the radius of the cationic motif varies from 7.719 Å of **Cd_8Cl** to 7.771 Å of **Cd_8Br** and finally to 7.796 Å of **Cd_8I**. The augmentation of the cluster size is partly attributed to the increase in Cd_i–X distances (Table S3). The variation in the type of counter anion of the **Cd_8X** NCs is associated with a change in the space group from $I4_1/a$ to $R\bar{3}c$, as evidenced by the distinctly different PXRD profiles of **Cd_8Cl** compared with those of the other two NCs (Fig. S4). As for the isomorphic **Cd_8Br** and **Cd_8I**, a majority of the PXRD peaks of **Cd_8I** are shifted towards smaller diffraction angles due to the larger sizes of both **Cd_8I** cation and $CdI_4{}^{2-}$ anion. Additionally, the high air stability of these **Cd_8X** NCs was confirmed, as no perceptible differences were observed between their PXRD patterns before and after exposure to ambient air for 24 h (Fig. S5). The EDX elemental analysis for **Cd_8X** samples showed that the element content ratios of Cd to halogen align with the results obtained from single-crystal X-ray diffraction studies (Fig. S6–S8).

Once the crystals of corresponding **Cd_8X** NCs began to precipitate, their mother liquors were immediately analyzed by ESI-MS to investigate the water robustness of the intact Cd_8 skeleton. Unfortunately, no MS signals due to the whole cationic skeleton of **Cd_8Cl** and **Cd_8Br** were detected, and the highest m/z peak for these two NCs was found at 1170.91 and 1214.86, respectively, corresponding to the tetranuclear species $[Cd_4(tacntp)_2X]^+$ (X = Cl or Br) (Fig. S9 and Table S4). By contrast, the intact octanuclear motif of **Cd_8I** could be preserved in aqueous solution, signified by the occurrence of the MS peak of $[Cd_8(tacntp)_4(OH)I]^{2+}$ at $m/z = 1206.40$ besides the identified segments ranging from mononuclear to tetranuclear species. On account of the higher water stability of **Cd_8I**, the time-resolved ESI-MS data were recorded over seven consecutive days to track its assembly process (Fig. 2a). On mixing the starting reagents, an ion peak was immediately observed at $m/z = 502.05$ corresponding to a sodium ion adduct of Cd^{II} metalloligand, $[Na_2Cd(tacntp)]^+$; meanwhile, the major peak appearing at $m/z = 679.98$ was assigned as the dinuclear Cd^{II} species $[Na_2Cd_2(tacntp)(OH)_2(CH_3OH)]^+$. As expected, tetranuclear Cd^{II} species $[Cd_4(tacntp)_2]^{2+}$ at $m/z = 566.97$ was assembled through the fusion of the established dinuclear Cd^{II} species. At the higher m/z region of 1100–1300, the signals with $z = 1$ charge state were present at $m/z = 1150.95$, 1195.93, 1222.97 and 1260.85, attributable to the tetranuclear Cd^{II} segments $[Cd_4(tacntp)_2(OH)]^+$, $[Cd_4(tacntp)_2(NO_3)]^+$, $[NaCd_4(tacntp)_2(OH)_2(CH_3OH)]^+$ and $[Cd_4(tacntp)_2I]^+$, respectively. At this time, no cluster fragments with higher nuclearity were found and the I^--containing species $[Cd_4(tacntp)_2I]^+$ can be regarded as the crucial intermediate for the further evolution into **Cd_8I** (Fig. 2b, S10 and Table S5). With a prolonged reaction time, the intensities of the MS signals arising from the tetranuclear Cd^{II} intermediates gradually increased, and $[Cd_4(tacntp)_2I]^+$ became the dominant species on the sixth day, accompanied by the suppressed MS peaks of mononuclear and dinuclear species. Apparently, tetranuclear Cd^{II} species were afforded at the expense of the depletion of those lower nuclearity intermediates. On the seventh day, some transparent crystals of **Cd_8I** were formed, and the dinuclear Cd^{II} species became the preferred species again. The drastic decrease in the peak intensities of tetranuclear segments might be attributed to the combination of iodide-free tetranuclear species with $[Cd_4(tacntp)_2I]^+$ into the intact cluster skeleton, which precipitated immediately due to the poor aqueous solubility. Fortunately, an MS peak attributed to the intact octanuclear dication $[Cd_8(tacntp)_4I(OH)]^{2+}$ could be detected at $m/z = 1206.40$ after zooming in the MS spectrum in the m/z range of 1140 and 1280. The ESI-MS analysis explicitly mapped out a stepwise evolution

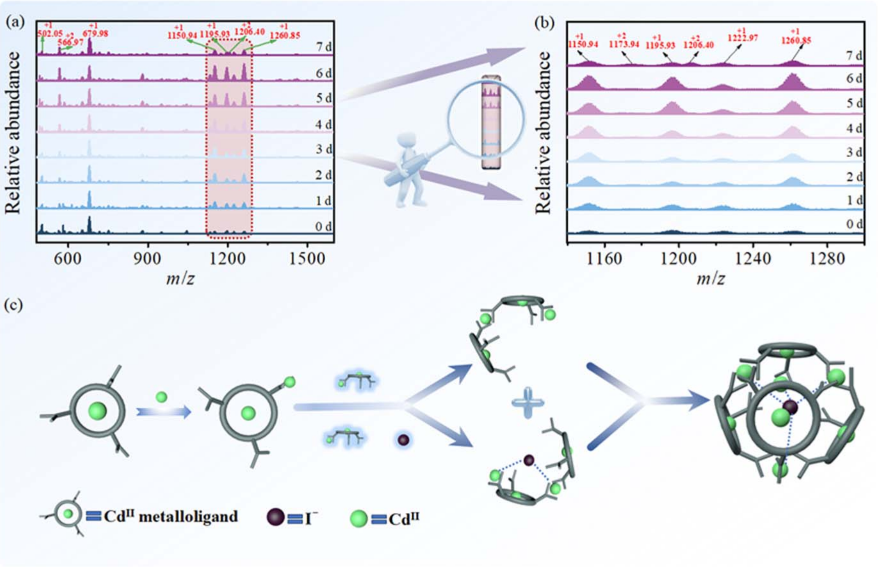

Fig. 2 (a) The time-resolved ESI-MS spectra of the reaction solution during the assembly of Cd_8I. (b) The local magnified ESI-MS images in the m/z range of 1100–1300. (c) The proposed assembly mechanism of Cd_8I.

pathway for **Cd_8I**: Cd_1 metalloligand → Cd_2 intermediate → Cd_4 and I@Cd_4 intermediates → **Cd_8I** skeleton (Fig. 2c). In CH_3OH, **Cd_8Cl** exhibited enhanced solution stability, and the Cl^--stabilized octanuclear cation was monitored as the predominant species in the MS spectrum (Fig. S11 and Table S6). Nevertheless, MS signals from **Cd_8Br** and **Cd_8I** could not be detected due to their insolubility in CH_3OH.

Such a halide-supported **Cd_8X** library prompts us to explore the templating effect of different halide ions through a competitive halide binding assay. When the nanocluster was prepared following the aforementioned procedure—except that the pure potassium halide was replaced by a mixture of equimolar amounts of KCl, KBr and KI—colorless crystals with irregular shape were deposited and collected. The EDX measurement for the as-synthesized crystalline samples verified the uniform distribution of Cl, Br and I elements on their surface. However, the content of I is greater than that of the other two halogen elements, with the I : Br : Cl molar content ratio of 2.51 : 0.92 : 0.66 (Fig. S12). The I^- selectivity is noticeable, tentatively ascribed to the consequence of soft–soft acid–base interaction and size-matching between the intra-cavity of the Cd_4^{inner} tetrahedron and the encapsulated anion. The size-dependent templating effect of halide ions on **Cd_8X** NC stabilization was further probed *via* template ion exchange experiments. After dispersing 0.1 mmol ground powder of **Cd_8Cl** in CH_3OH solution containing three equivalents of KBr or KI, the mixture was then kept under ambient conditions with stirring for one week. The resulting solids were collected and evaluated by PXRD analysis. The complete disappearance of the characteristic diffraction peaks for **Cd_8Cl** and the good agreement of the experimental PXRD pattern with that of either **Cd_8Br** or **Cd_8I** undoubtedly confirm the successful conversion of **Cd_8Cl** to the other two **Cd_8X** NCs *via* halide ion exchange. Likewise, I^- can substitute for Br^- wrapped in the cavity of **Cd_8Br**. On the contrary, **Cd_8I** dispersed in CH_3OH solution, including three equivalents of KCl or KBr, could not afford the corresponding halide-exchanged product (Fig. S13). Obviously, the halide encapsulation preference by the bitetrahedral NCs follows the size order of halide ions: $I^- > Br^- > Cl^-$.

It is conceivable that the Cd^{II} metalloligand present in **Cd_8X** may be an appropriate surface-protecting ligand for Ag NCs for the following two reasons: (1) the tripodally arranged pendant arms with abundant carboxylate O sites are available for $Ag^{0/I}$ binding, and (2) the flexible orientation of the pendant arms relative to the macrocyclic backbone favors the formation of geometrically matching O-donor triads for passivating the surface Ag_3 trigons of Ag NCs with convex polyhedral skeletons. Meanwhile, the appropriate solution stability of **Cd_8Cl** suggests that it can be used as a precursor to access heterometallic Ag NCs through structural transformation. First, it could be hypothesized that such a precursor nanocluster can release free metalloligands through the abstraction of halide ions by Ag^I. Subsequently, the released metalloligand can adopt the robust face-capping modes to steer the construction and protection of the polyhedral Ag kernel. To realize the above concept, 2.85×10^{-3} mmol of **Cd_8Cl** was dissolved in 5 mL of CH_3OH by the addition of 50 equivalents of $AgNO_3$, and then the mixed solution was exposed to the ambient environment. After three days, a small amount of brown solid was precipitated from the solution (Fig. S14). PXRD analysis revealed that the precipitate (referred to as **Cd_8Cl_$AgNO_3$**) is a mixture of AgCl and elemental Ag, along with some unidentified substances (Fig. S15), indicating that the Cl^- ion was abstracted from **Cd_8Cl** by $AgNO_3$. Then, ESI-MS analysis was performed on the reaction supernatant to uncover the skeleton robustness of the octanuclear Cd^{II} cluster free of Cl^-. Unexpectedly, no MS signals due to Cd_8 species could be detected in the positive-ion mode, and mono-charged peaks corresponding to several Ag^I-bound oligonuclear species, such as $[Ag_2Cd(tacntp)]^+$, $[Ag_2Cd(tacntpH)(NO_3)(CH_3OH)]^+$, $[Ag_3Cd(tacntp)Cl]^+$ and $[Ag_3Cd(tacntp)(NO_3)(CH_3OH)]^+$, were detected at *m*/*z* = 669.87, 764.92, 813.75, and 872.82, respectively (Fig. S16a and Table S7). Apparently, $AgNO_3$ triggers the disintegration of **Cd_8Cl**, and then the released $[Cd(tacntp)]^-$ metalloligand binds to Ag^I to produce some polynuclear Cd–Ag species. The destruction of the **Cd_8Cl** skeleton was also confirmed by the dominant peak (*m*/*z* = 456.07) ascribed to the solo metalloligand found in the negative-ion mode MS spectrum (Fig. S16b). More interestingly, the supernatant is yellow-emissive under 302 nm UV irradiation. In addition, the steady-state fluorescence measurement revealed that the supernatant shows a broad emission peak centered around 556 nm, which is essentially independent of the excitation wavelength (Fig. S17). This confirmed the homogeneity of the photoluminescent components within the supernatant. TEM investigation showed the presence of small, well-dispersed particles in the supernatant with an average size of approximately 2.31 nm (Fig. S18). On the slow diffusion of ethyl acetate into the supernatant under ambient conditions, rod-like brown-red single crystals of **Cd_7Ag_{21}** NC were obtained and structurally elucidated (Fig. S19).

The overall chemical composition of **Cd_7Ag_{21}** inferred by single-crystal X-ray diffraction analysis was formulated as $[Ag_{21}Cd_7(tacntp)_7(NO_3)_2](NO_3)_2\cdot Cl_2\cdot 14H_2O$. The crystallographic data and structure refinement parameters for **Cd_7Ag_{21}** are listed in Table S8, and the selected bond lengths and angles are included in Table S9. The nanocluster comprises an Ag_{20} kernel shielded by seven face-capping Cd^{II} metalloligands with Ag–O bond lengths in the range of 2.21(2)–2.590(15) Å. An extra $Ag(NO_3)_2^-$ unit is left at the periphery of the nanocluster, which is tethered to the inner Ag_{20} core *via* one pendant carboxylate group of a metalloligand (Fig. 3a). As expected, the diameter of the intact cationic unit of **Cd_7Ag_{21}** is about 2.2 nm, which is comparable to the size of the luminescent particles present in the supernatant during the conversion process. The Ag_{20} core features a centered Ag_{13} icosahedron with the remaining seven Ag atoms constituting a three-petal-like receptacle to accommodate the icosahedron (Fig. 3b). Argentophilic interactions are pivotal to keep the twenty Ag atoms together corroborated by the fact that the radial and peripheral Ag–Ag separations in the Ag_{13} icosahedron vary between 2.723(2)–2.894(2) Å and 2.766(2)–3.220(2) Å, respectively, and those in the receptacle lie in the range of 2.728(3)–3.002(2) Å. Six metalloligands with a staggered six-membered ring arrangement act as fasteners to join the icosahedron and its receptacle, besides the Ag–Ag interactions (2.728(3)–3.025(2)) Å between icosahedral and receptacle Ag

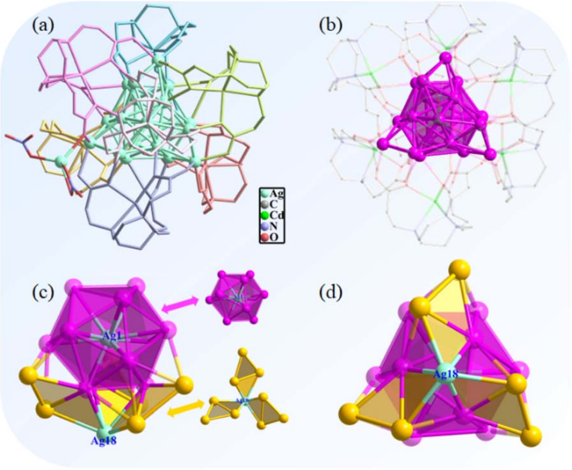

Fig. 3 Surface arrangement of Cd^{II} metalloligands (a) and the inner Ag_{20} core featuring a centered Ag_{13} icosahedron (b) in $\mathbf{Cd_7Ag_{21}}$. Side view (inset: Ag_{13} icosahedron and its receptacle) (c) and top view (d) of the Ag_{20} core in $\mathbf{Cd_7Ag_{21}}$ with the quasi-C_3 axis passing through Ag_1 and Ag_{18} atoms. Color codes: purple, yellow and light-green spheres, Ag; green sphere, Cd; red sphere, O; lilac sphere, N; gray sphere, C.

atoms). A quasi-C_3 axis passes through the central Ag_{18} atom of the receptacle and the Ag_1 center within the Ag_{13} icosahedron, and each petal of the receptacle consists of an Ag_2 pair being disposed clockwise about the axis; therefore, the Ag_{20} core is essentially chiral (Fig. 3c and d). As each metalloligand possesses six O donors (three of them orient inwards to coordinate with the Cd^{II} center and the other three orient outwards as free donors) for potential Ag binding, the moderate flexibility of its propionate pendant arms provides the chance to adjust their orientation and thus the separations between O donors. This is conducive for the metalloligand to shield more Ag_3 triangles on the surface of the Ag_{20} core. Notably, four different binding motifs are exhibited by seven passivating Cd^{II} metalloligands (denoted as ML_{Cd}) based on their connectivity to Ag atoms. ML_{Cd_1}, ML_{Cd_2} and ML_{Cd_5} assume a (λλλ) conformation on their macrocyclic backbone, and one propionate pendant arm is oriented anticlockwise with respect to the backbone, but the other two are oriented clockwise. The six O donors of each these metalloligands chelate five Ag atoms, by which three Ag_3 triangles are generated *via* edge-sharing. Among these trigons, two are capped by three inward and one outward O atoms, while the other is mounted by one inward and two outward O atoms (motif I). ML_{Cd_3}, ML_{Cd_6} and ML_{Cd_4} feature the same backbone conformation and similar arrangement of the pendant arms to the above metalloligands. Differently, ML_{Cd_3} and ML_{Cd_6} bridge six Ag atoms stemming from four edge-shared Ag_3 triangles. Two of four Ag_3 trigons are protected by one inward and two outward O atoms, the third trigon is only connected to three inward O atoms, and the remaining one is covered by two inward and one outward O atoms (motif II). The coordination pattern of ML_{Cd_4} is analogous to motif II, and the only discrepancy is that one outward O-donor functions as a μ_2 bridge, linking an additional Ag21 atom (motif III). The backbone of ML_{Cd_7} adopts a (δδδ) conformation, and three pendant arms are all oriented anticlockwise. It serves as a capping shell for four Ag atoms in an Ag_4 triangular pyramid with Ag–Ag contacts between the apex and base atoms, revealing a coordination mode quite different from that of motifs I–III. Each of the three Ag_3 lateral surfaces (viewed as the pseudo-surface Ag_3 trigon) of the triangular pyramid is connected to two inward and two outward O atoms of ML_{Cd_7} (motif IV) (Fig. 4 and S20). Thanks to the perfect passivation of the macrocyclic metalloligands for the Ag_3 triangular face, the Ag_{20} core with 34 edge-shared surface Ag_3 trigons can be stabilized. Because of the chirality of the metallic core and the asymmetric anchoring of chiral metalloligands on its surface, an individual cationic cluster unit of $\mathbf{Cd_7Ag_{21}}$ is chiral. However, equivalent enantiomers are packed in a single crystal and therefore, $\mathbf{Cd_7Ag_{21}}$ is a racemate, crystallizing in a centrosymmetric triclinic space group, $P\bar{1}$. Moreover, the homogeneous phase of the as-prepared $\mathbf{Cd_7Ag_{21}}$ during the nanocluster transformation process was determined by the PXRD analysis. After being exposed to air for 24 h, the observed line broadening of the PXRD patterns of $\mathbf{Cd_7Ag_{21}}$ seems to originate from a partial loss of crystallinity (Fig. S21).

The XPS survey spectrum suggested that $\mathbf{Cd_7Ag_{21}}$ consists of C, N, O, Cl, Ag and Cd elements (Fig. S22a). The narrow-scan Ag 3d spectrum showed two peaks at binding energies of 373.76 eV and 367.79 eV, which could be deconvoluted into four sub-bands (Fig. S22b). These sub-bands indicate the presence of metallic Ag^0 and Ag^I in the nanocluster (373.62 and 367.70 eV for Ag^I $3d_{3/2}$ and $3d_{5/2}$, 374.25 and 368.22 eV for Ag^0 $3d_{3/2}$ and $3d_{5/2}$);[24,45,46] hence, $\mathbf{Cd_7Ag_{21}}$ was proven to be a superatomic species. The free valence electron number was calculated as 8 $\{n = 21 - 7 - 2 - 4\}$,[47] which fills a closed electronic shell of $1S^2 1P^6$ based on a jellium model. The photophysical properties of $\mathbf{Cd_7Ag_{21}}$ in CH_3OH were further investigated. The UV-visible absorption spectrum of the nanocluster showed two absorption peaks at 342 and 391 nm, and the latter is close to its

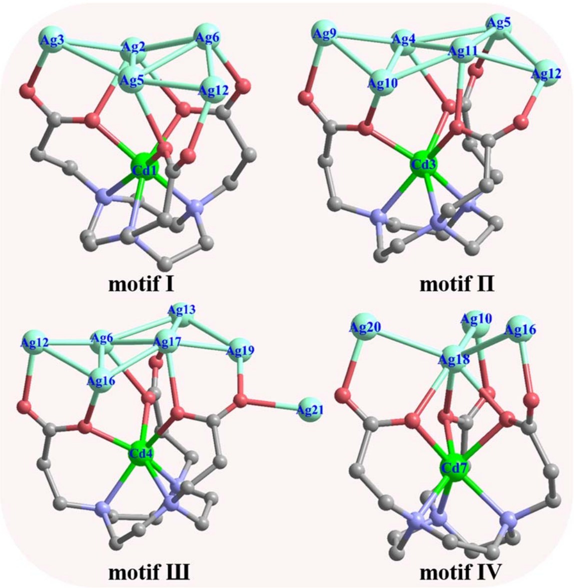

Fig. 4 Schematic representation of the binding modes of Cd^{II} metalloligands to surface Ag_3 trigons in $\mathbf{Cd_7Ag_{21}}$.

optimal excitation wavelength (Fig. S23). Considering the relatively weak affinity of Cd^{II} metalloligands to the Ag_{20} core, the 556 nm emission of $\mathbf{Cd_7Ag_{21}}$ under 396 nm excitation might be tentatively ascribed to cluster core-centered charge transfer. The skeleton rigidity of the Ag_{20} kernel imposed by the peripheral metalloligands contributes to the intense yellow photoluminescence of $\mathbf{Cd_7Ag_{21}}$. The short lifetime of 1.52 ns is indicative of fluorescence decay characteristics, and the total quantum yield is 1.53% (Fig. S24). Moreover, the remarkable stability of $\mathbf{Cd_7Ag_{21}}$ in CH_3OH was indicated by the unchanged fluorescence intensity of this solution after storing under ambient conditions for one week (Fig. S25). Conversely, the excellent photophysical stability of the methanolic solution of $\mathbf{Cd_7Ag_{21}}$ means that it has great potential in fluorescence sensing.

A series of control experiments was conducted and fluorescently monitored to determine the key factors that drive the generation of fluorescent $\mathbf{Cd_7Ag_{21}}$. First, it should be noted that neither starting reagents used to prepare $\mathbf{Cd_8Cl}$ nor $\mathbf{Cd_8Cl}$ itself exhibited yellow fluorescence under a 302 nm UV lamp (Fig. S26a). Upon treatment with $AgNO_3$, the $\mathbf{Cd_8Cl}$ solution became luminous after 2 hours of exposure to natural light, and the emission gradually enhanced in the next three days (Fig. S26b and S27). Moreover, the production of $\mathbf{Cd_7Ag_{21}}$ could be accelerated by UV light, and the emission brightness of the reaction supernatant reached a maximum within 30 min of irradiation at 302 nm (Video in SI). For comparison, a mixed solution of $\mathbf{Cd_8Cl}$ and $AgNO_3$ kept in the dark for three days only showed insignificant fluorescence (Fig. S28), which indicated that $\mathbf{Cd_7Ag_{21}}$ can only be accessed *via* a photochemical process. Second, the critical role of the choice of $\mathbf{Cd_8X}$ precursor for the preparation of the target Ag NC was evaluated. When substituting $\mathbf{Cd_8Br}$ for $\mathbf{Cd_8Cl}$ as the precursor, while the other reaction conditions were kept constant, the supernatant of the reaction mixture emitted only a faint yellow fluorescence under a 302 nm lamp. The large amount of brown precipitate (referred to as $\mathbf{Cd_8Br}$_$AgNO_3$) at the bottom of the container was identified as AgBr *via* PXRD analysis, as well as some unidentified amorphous products (Fig. S29a). If $\mathbf{Cd_8I}$ was applied as the precursor, no luminescent nanostructures could be obtained during the whole reaction period, and the as-formed pale-yellow precipitate (referred to as $\mathbf{Cd_8I}$_$AgNO_3$) was recognized as Ag_2INO_3 (*i.e.*, a mixed phase of $AgNO_3$ and AgI) (Fig. S29b). These observations demonstrated that $\mathbf{Cd_8Br}$ and $\mathbf{Cd_8I}$ tend to form AgX precipitates rather than $\mathbf{Cd_7Ag_{21}}$ when treated with $AgNO_3$. Third, a mixture of $tacntpH_3$, $AgNO_3$ and KCl dissolved in CH_3OH with a molar ratio of 4 : 50 : 1 subjected to 30 min of UV irradiation was non-fluorescent (Fig. S30). The inability of $tacntpH_3$ to produce fluorescent NCs might arise from the random orientation of carboxylate pendant arms, preventing the free macrocyclic ligand from effectively mediating the formation of the Ag core and the passivation of its surface. If $tacntpH_3$ was replaced by the preformed metalloligand (a mixed solution of equimolar $tacntpH_3$ and Cd^{II} in CH_3OH), the irradiated mixture exhibited a faint blue emission (Fig. S31). The TEM analysis for the collected nanostructures showed the particles with an average size (1.71 nm) smaller than that of $\mathbf{Cd_7Ag_{21}}$ (Fig. S32). Evidently, $\mathbf{Cd_8Cl}$ as a carrier of Cd^{II} metalloligand plays a determining role in the directed assembly of $\mathbf{Cd_7Ag_{21}}$. Fourth, the unique regulatory effect of $\mathbf{Cd_8Cl}$ on the light-induced synthesis of $\mathbf{Cd_7Ag_{21}}$ was further evaluated by deliberately varying the molar ratio of $AgNO_3$ and $\mathbf{Cd_8Cl}$ from 1 : 1 to 300 : 1 (Fig. S33–S36). After UV illumination, the resulting reaction supernatants were sampled and analyzed through TEM. It is worth noting that a few non-fluorescent Ag NPs larger than 10 nm were fabricated at the lowest molar ratio of 1 : 1. When the molar ratio of $AgNO_3$ to $\mathbf{Cd_8Cl}$ was either 10 : 1 or 150 : 1, the supernatant emitted a weak green/yellowish green fluorescence. The particles were polydisperse in size, consisting of a mixture of non-fluorescent Ag NPs and fluorescent $\mathbf{Cd_7Ag_{21}}$. When the molar ratio of $AgNO_3$ to $\mathbf{Cd_8Cl}$ was increased to 300 : 1, the supernatant became non-luminous again, and the dense Ag nanostructures in this supernatant had a wide size distribution ranging from 2 to 8 nm. Only at a molar ratio of 50 : 1 for $AgNO_3$ to $\mathbf{Cd_8Cl}$ was the highest emission brightness observed for the supernatant, in which uniform-sized $\mathbf{Cd_7Ag_{21}}$ NCs were stabilized. Fifth, additional comparative experiments revealed that yellow-emissive $\mathbf{Cd_7Ag_{21}}$ NCs can only be prepared through the light-induced reaction in CH_3OH or a mixture of CH_3OH/CH_3CH_2OH or CH_3OH/DMF (v/v = 1/1) (Fig. S37), evidencing that CH_3OH is indispensable for the conversion of $\mathbf{Cd_8Cl}$ to $\mathbf{Cd_7Ag_{21}}$. These findings raise the question as to whether CH_3OH functions as a reducing agent for Ag^I in this conversion. However, after the light-induced conversion of $\mathbf{Cd_8Cl}$ in CH_3OH, corresponding oxidation products (*e.g.* HCHO and HCOOH) of CH_3OH could not be detected in the reaction mixture by ion chromatography and ^{13}C-NMR, and EPR measurement using PBN as a spin trap failed to observe the resonance signal produced from the reductive hydroxymethyl radical (Fig. S38).[48,49] Consequently, there was no direct evidence to suggest that CH_3OH acts as a reducing agent during the nanocluster conversion process. Finally, the impact of reaction temperature on the light-induced conversion of $\mathbf{Cd_8Cl}$ was investigated under natural light at the optimal molar ratio of $AgNO_3$ and $\mathbf{Cd_8Cl}$. At temperatures of 25 and 40 °C, the luminous intensity of the reaction supernatants was independent of temperature, and the formation yield of $\mathbf{Cd_7Ag_{21}}$ remained constant. As the temperature was raised above 50 °C, the yellow emission intensity of the supernatants dropped with the increasing temperature, accompanied by a decreasing yield of $\mathbf{Cd_7Ag_{21}}$ as well as an increasing amount of black precipitate (suspected to be silver particles) (Fig. S39 and S40). Based on the above investigations, the photochemical synthesis mechanism of $\mathbf{Cd_7Ag_{21}}$ was supposed as follows: (1) $\mathbf{Cd_8Cl}$ experiences an Ag^I-triggered cluster disassembly to provide Ag^I-anchored metalloligands. (2) Light-induced partial reduction of Ag^I ions bound to the metalloligand and the subsequent fusion of the metalloligand-bound silver species *via* Ag–carboxylate coordination and argentophilic interaction to shape the Ag kernel. (3) Full surface coverage of metalloligands on the established Ag kernel to restrict its further growth or aggregation (Fig. 5). Notably, $\mathbf{Cd_8Cl}$ as a slow-releasing carrier of $[Cd(tacntp)]^-$ provides a unique environment for light-induced reduction of Ag^I together with a preferable concentration ratio of

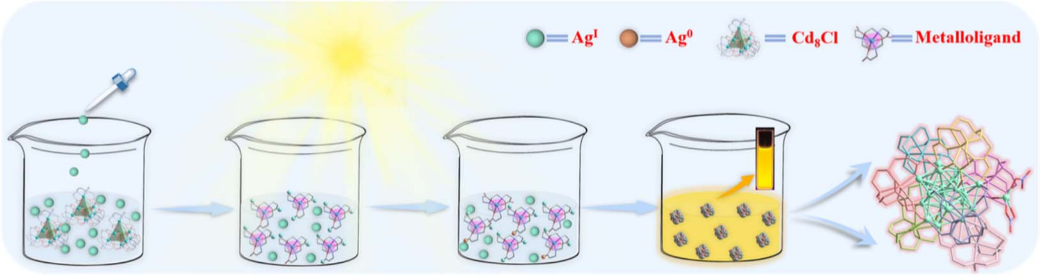

Fig. 5 Schematic diagram of the transformation process from $\mathbf{Cd_8Cl}$ to $\mathbf{Cd_7Ag_{21}}$.

metalloligand to Ag^I, which is beneficial for the creation of fluorescent Ag NCs with excellent monodispersity in an otherwise unattainable chemical microenvironment.

A few photoluminescent Ag NCs have been developed as sensitive and selective sensors for thiol-containing amino acids such as Cys due to the strong affinity of thiol groups with the Ag NC surface.[50–53] On the basis of soft and hard acid–base theory, as a hard base, the tripodal metalloligand with all carboxylate binding sites may exhibit relatively weaker interaction with soft-acid Ag ion/atom of Ag NCs than thiol-containing compounds. Thus, the as-prepared $\mathbf{Cd_7Ag_{21}}$ was expected to be applicable for detecting thiol-containing substrates through ligand-exchange-induced fluorescence change. Upon adding 80 μM of Cys to a methanolic solution of $\mathbf{Cd_7Ag_{21}}$ at a concentration of 55 μM, the kernel-based emission was quenched to about 15% of the original intensity, accompanied by a blue shift of the emission maximum from 556 to 534 nm (Fig. 6a and b). Under a UV lamp, the complete disappearance of the yellow photoluminescence of $\mathbf{Cd_7Ag_{21}}$ when Cys was present further evidenced the quenching ability of $\mathbf{Cd_7Ag_{21}}$ by Cys. The quenching efficiency of Cys on $\mathbf{Cd_7Ag_{21}}$ was linearly related to the concentration of Cys in the range of 60–80 μM ($R^2 = 0.9941$), and the quenching constant K_{SV} was calculated to be 1.51×10^5 M^{-1}, with a detection limit as low as 0.16 μM (Fig. S41). The detection sensitivity of $\mathbf{Cd_7Ag_{21}}$ for Cys is comparable to that of some existing coinage metal NCs (Table S10).

Some analyses were conducted for the $\mathbf{Cd_7Ag_{21}}$ sample after Cys treatment (referred to as $\mathbf{Cd_7Ag_{21}}$_Cys) to make clear the quenching mechanism of Cys for the emission of $\mathbf{Cd_7Ag_{21}}$. After sensing Cys, the Tyndall effect of the sample solution became

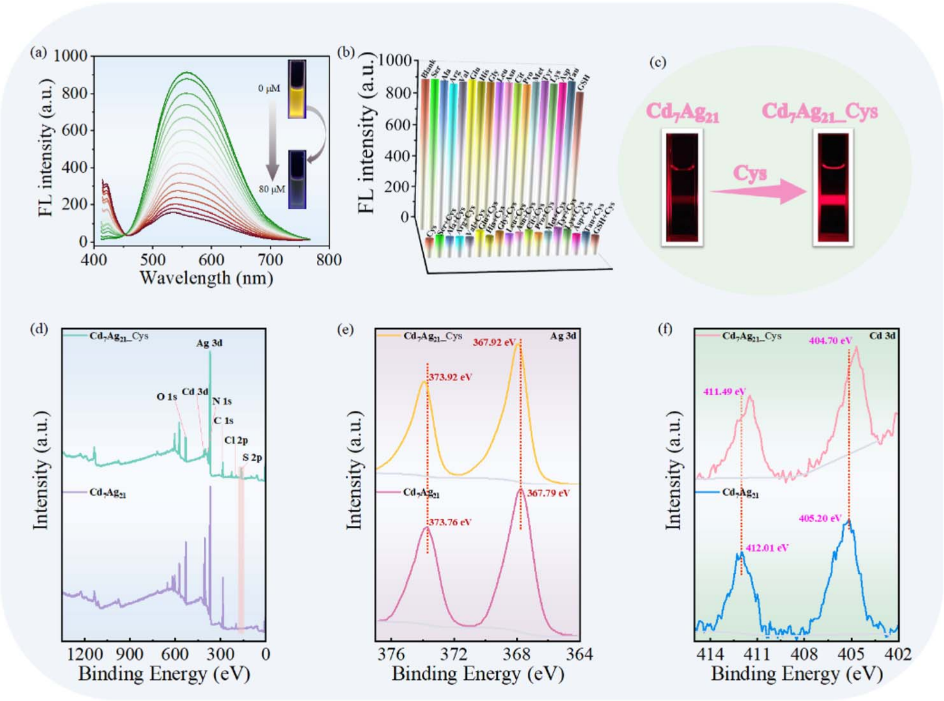

Fig. 6 (a) Emission spectra ($\lambda_{ex} = 396$ nm) of $\mathbf{Cd_7Ag_{21}}$ in the presence of different concentrations of Cys (inset showing images of the fluorescence change of $\mathbf{Cd_7Ag_{21}}$ before and after addition of 80 μM of Cys). (b) Fluorescence response of $\mathbf{Cd_7Ag_{21}}$ dissolved in CH_3OH to 100 μM of different interfering substances in the absence and presence of 80 μM Cys. (c) Optical images of the Tyndall effect of a methanol solution of $\mathbf{Cd_7Ag_{21}}$ before and after the addition of 80 μM of Cys. (d) XPS survey spectra of $\mathbf{Cd_7Ag_{21}}$ and $\mathbf{Cd_7Ag_{21}}$_Cys. (e) XPS high-resolution spectra of Ag 3d for $\mathbf{Cd_7Ag_{21}}$ and $\mathbf{Cd_7Ag_{21}}$_Cys. (f) XPS high-resolution spectra of Cd 3d for $\mathbf{Cd_7Ag_{21}}$ and $\mathbf{Cd_7Ag_{21}}$_Cys.

more obvious (Fig. 6c), which tentatively proved the larger size of **Cd_7Ag_{21}_Cys**. Subsequent TEM results further confirmed that the average diameter of **Cd_7Ag_{21}_Cys** particles approaches 20 nm, larger than that of **Cd_7Ag_{21}** (Fig. S42). The EDX mapping of Ag showed that this element is homogeneously present on the surface of the obtained nanoparticles, as is the S element from the exogenous Cys (Fig. S43). In addition, the full XPS spectrum clearly showed that **Cd_7Ag_{21}_Cys** is composed of C, N, O, S, Cl, Cd, and Ag elements (Fig. 6d). The binding energies of Ag doublets were positively shifted to 373.92 and 367.92 eV, indicating that Ag might interact with the sulfhydryl group of Cys (Fig. 6e). The peak at 162.08 eV in the high-resolution spectrum was attributed to S 2p, reconfirming the presence of Ag–S interactions (Fig. S44).[54–56] Furthermore, the positions of the Cd $3d_{3/2}$ and Cd $3d_{5/2}$ signals were significantly shifted to higher binding energies, so Cys might also abstract Cd^{II} from the metalloligand (Fig. 6f).[57–59] Therefore, a possible interpretation for the Cys-induced fluorescence quenching is that Cys may destabilize **Cd_7Ag_{21}** by partially/completely replacing the metalloligands anchored on its surface. Then the inferior coverage of Cys for the Ag kernel leads to the agglomeration of these Cys-protected Ag NCs into non-luminous Ag NPs with a larger size. The disappearance of the corresponding –SH stretching vibration band of Cys at 2550 cm^{-1} in the FT-IR spectrum of **Cd_7Ag_{21}_Cys** provided another support that Cys was anchored to silver NPs *via* Ag–S bonds (Fig. S45).[60–62] ESI-MS analysis of a methanol solution of **Cd_7Ag_{21}** after Cys treatment was conducted to gain direct information for Cys replacement. Peaks corresponding to the complete skeleton of **Cd_7Ag_{21}**, as well as the fragments containing metalloligand could not be identified in the mass spectrum, but instead a peak found at *m*/*z* 346.20 could be attributed to the mono-protonated macrocyclic ligand, which arose from the Cys-induced destruction of the metalloligand (Fig. S46). The presence of the free ligand in the solution indirectly proved that the aggregation of Ag NCs into non-fluorescent NPs occurs after surface ligand exchange. The proposed mechanism was further corroborated by the quenching effects of some alkyl thiols (EtSH, 1-PrSH and *t*-BuSH) towards the yellow fluorescence of **Cd_7Ag_{21}** (Fig. S47). The quenching efficiency of these quenchers decreased in the order *t*-BuSH > 1-PrSH > EtSH, which coincides with their Ag-binding affinity depending on the electron-donating ability of alkyl groups of thiols.

Particularly, the assay is specific for the detection of Cys among seventeen selected amino acids, including two other S-containing amino acids, methionine (Met) and taurine (Tau), as well as glutathione (GSH, a tripeptide containing Cys moiety). All other analytes barely showed turn-off effects on the fluorescence of **Cd_7Ag_{21}** even at a concentration equal to 100 μM. Moreover, none of them could apparently disturb the quenching ability of Cys for **Cd_7Ag_{21}** (Fig. 6b). The inability of GSH, Met or Tau to turn off the fluorescence of **Cd_7Ag_{21}** might be ascribed to the following aspects: the less exposed thiol group of GSH, the bulky methyl group attached to the sulfur atom of Met, and the oxygen atoms surrounding the sulfur atom of Tau preclude these substances from replacing the metalloligands anchored on the surface of **Cd_7Ag_{21}** through Ag–S bonds, and thus the destabilization and agglomeration of small-sized Ag NCs into non-luminous NPs could not occur.

Conclusion

In summary, Ag^I triggers the light-induced structural transformation of a chloride-centered bitetrahedral **Cd_8Cl** nanocluster into a yellow-emissive heterometallic **Cd_7Ag_{21}** nanocluster featuring an icosahedron-based Ag_{20} kernel. The Cd^{II} macrocyclic metalloligand released from **Cd_8Cl** behaves as a powerful structure-directing agent by face-capping on the surface Ag_3 trigons to achieve the shaping and protection of the metallic kernel. Meanwhile, the precursor nanocluster as a carrier of metalloligands supplies an appropriate chemical microenvironment for the nanocluster conversion. The labile coordination between the metalloligands and surface Ag ions/atoms of **Cd_7Ag_{21}** provides the fluorescent nanocluster with the inherent capability to selectively recognize Cys through switch-off response deriving from ligand replacement-cluster aggregation. Further efforts are focused on metalloligand tailoring to improve the controllability of metalloligand-mediated cluster transformation to target heterometallic NCs with designed structures and attractive properties suitable for versatile applications.

Author contributions

Biliu Lan: investigation, methodology, data curation, writing – original draft, review & editing. Ziling Li: investigation, data curation. Yanfang Feng: investigation. Tao Deng: data curation. Min Pan: investigation. Zhong Zhang: supervision, conceptualization, writing – review & editing, funding acquisition.

Conflicts of interest

The authors declare that they have no known competing financial interests or personal relationships that could have appeared to influence the work reported in this paper.

Data availability

CCDC 2464348–2464351 contain the supplementary crystallographic data for this paper.[63a–d]

The data supporting this article have been included as part of the supplementary information (SI). Supplementary information: materials and instruments, experimental section and additional figures and tables; FT-IR spectra, PXRD profiles, TEM images, ESI-MS spectra, UV-vis absorption spectra, emission spectra, photoluminescence lifetime decay curve, EPR spectra, XPS spectra, crystal structure images, crystal data tables, and performance comparison table for Cys detection; a video showing the fluorescence change of the reaction supernatant during 30 min UV irradiation. See DOI: **https://doi.org/10.1039/d5sc04963f**.

Acknowledgements

This work was financially supported by the National Natural Science Foundation of China (21861003).

References

1 Y. Z. Huang, R. K. Gupta, G. G. Luo, Q. C. Zhang and D. Sun, Luminescence thermochromism in atomically precise silver clusters: A comprehensive review, *Coord. Chem. Rev.*, 2024, **499**, 215508.

2 M. Yang, L. Zhu, W. Yang and W. Xu, Nucleic acid-templated silver nanoclusters: A review of structures, properties, and biosensing applications, *Coord. Chem. Rev.*, 2023, **491**, 215247.

3 S. Qian, Z. Wang, Z. Zuo, X. Wang, Q. Wang and X. Yuan, Engineering luminescent metal nanoclusters for sensing applications, *Coord. Chem. Rev.*, 2022, **451**, 214268.

4 X. Kang, Y. Li, M. Zhu and R. Jin, Atomically precise alloy nanoclusters: syntheses, structures, and properties, *Chem. Soc. Rev.*, 2020, **49**, 6443–6514.

5 I. Chakraborty and T. Pradeep, Atomically precise clusters of noble metals: Emerging link between atoms and nanoparticles, *Chem. Rev.*, 2017, **117**, 8208–8271.

6 L. Liu, S. J. Zheng, H. Chen, J. Cai and S. Q. Zang, Tandem nitrate-to-ammonia conversion on atomically precise silver nanocluster/MXene electrocatalyst, *Angew. Chem., Int. Ed.*, 2024, **63**, e202316910.

7 L. Li, Y. Lv, H. Sheng, Y. Du, H. Li, Y. Yun, Z. Zhang, H. Yu and M. Zhu, A low-nuclear Ag_4 nanocluster as a customized catalyst for the cyclization of propargylamine with CO_2, *Nat. Commun.*, 2023, **14**, 6989.

8 Y. Xiao, Z. Wu, Q. Yao and J. Xie, Luminescent metal nanoclusters: Biosensing strategies and bioimaging applications, *Aggregate*, 2021, **2**, 114–132.

9 L. M. Zheng, W. Q. Shi, F. Hu, Z. J. Guan and Q. M. Wang, All-calixarene-protected silver nanocluster with all silver atoms in a face-centered cubic arrangement, *J. Am. Chem. Soc.*, 2024, **146**, 25101–25107.

10 C. Deng, C. Sun, Z. Wang, Y. Tao, Y. Chen, J. Lin, G. Luo, B. Lin, D. Sun and L. Zheng, A sodalite-type silver orthophosphate cluster in a globular silver nanocluster, *Angew. Chem., Int. Ed.*, 2020, **59**, 12659–12663.

11 T. Xu, S. Paul, C. Zhang, M. Azam, B. L. Han, W. D. Si, Z. Wang, Z. Y. Gao, A. Anoop, C. H. Tung and D. Sun, Boosting circularly polarized luminescent and decagram-scale mechanochemistry synthesis of atomically precise superstructure from achiral silver cluster and chiral cyclodextrin, *CCS Chem.*, 2025, **7**, 519–531.

12 S. Biswas, S. Das and Y. Negishi, Progress and prospects in the design of functional atomically-precise Ag(I)-thiolate nanoclusters and their assembly approaches, *Coord. Chem. Rev.*, 2023, **492**, 215255.

13 N. L. Li, J. Wei, X. Y. Ran, J. Li, L. Shen, F. Zhang, Q. Dai, W. Wang, K. Li and X. K. Wan, All-alkynyl protected rod-shaped $Au_9(AgCu)_{126}$ nanocluster with remarkable photothermal conversion, *Angew. Chem., Int. Ed.*, 2025, **64**, e202503036.

14 M. Qu, F. Q. Zhang, G. L. Zhang, M. M. Qiao, L. X. Zhao, S. L. Li, M. Walter and X. M. Zhang, Cocrystallization-driven formation of fcc-based Ag_{110} nanocluster with chinese triple luban lock shape, *Angew. Chem., Int. Ed.*, 2024, **63**, e202318390.

15 Y. X. Wang, J. Zhang, H. F. Su, X. Cui, C. Y. Wei, H. Li and X. M. Zhang, Photochemical synthesis of atomically precise Ag nanoclusters, *ACS Nano*, 2023, **17**, 11607–11615.

16 Q. Yao, T. Chen, X. Yuan and J. Xie, Toward total synthesis of thiolate-protected metal nanoclusters, *Acc. Chem. Res.*, 2018, **51**, 1338–1348.

17 A. Desireddy, B. E. Conn, J. Guo, B. Yoon, R. N. Barnett, B. M. Monahan, K. Kirschbaum, W. P. Griffith, R. L. Whetten, U. Landman and T. P. Bigioni, Ultrastable silver nanoparticles, *Nature*, 2013, **501**, 399–402.

18 C. Zhang, W. D. Si, W. D. Tian, W. J. Xiao, Z. Y. Gao, Z. Wang, C. H. Tung and D. Sun, Single-atom "surgery" on chiral all-dialkynyl-protected superatomic silver nanoclusters, *Sci. Bull.*, 2025, **70**, 365–372.

19 Z. Wang, F. Alkan, C. M. Aikens, M. Kurmoo, Z. Y. Zhang, K. P. Song, C. H. Tung and D. Sun, An ultrastable 155-nuclei silver nanocluster protected by thiacalix[4]arene and cyclohexanethiol for photothermal conversion, *Angew. Chem., Int. Ed.*, 2022, **61**, e202206742.

20 W. D. Tian, C. Zhang, S. Paul, W. D. Si, Z. Wang, P. P. Sun, A. Anoop, C. H. Tung and D. Sun, Lattice modulation on singlet-triplet splitting of silver cluster boosting near-unity photoluminescence quantum yield, *Angew. Chem., Int. Ed.*, 2025, **64**, e202421656.

21 K. Sheng, Z. Wang, L. Li, Z. Y. Gao, C. H. Tung and D. Sun, Solvent-mediated separation and reversible transformation of 1D supramolecular polymorphs built from $[W_{10}O_{32}]^{4-}$ templated 48-nuclei silver(I) cluster, *J. Am. Chem. Soc.*, 2023, **145**, 10595–10603.

22 R. Ge, X. X. Li and S. T. Zheng, Recent advances in polyoxometalate-templated high-nuclear silver clusters, *Coord. Chem. Rev.*, 2021, **435**, 213787.

23 W. H. Jiang, X. M. Zeng, M. Wu, L. Qin, L. Y. Yao and G. Y. Yang, Thermally activated delayed fluorescence-based near-infrared-II luminescence and controlled size growth of silver nanoclusters, *ACS Nano*, 2025, **19**, 7129–7139.

24 L. H. Hong, S. N. Yue, X. Huang, C. Sun, P. W. Cai, Y. Q. Sun, X. X. Li and S. T. Zheng, Development of stable water-soluble supratomic silver clusters utilizing a polyoxoniobate-protected strategy: Giant core-shell-type $Ag_8@Nb_{162}$ fluorescent nanocluster, *Angew. Chem., Int. Ed.*, 2024, **63**, e202404314.

25 F. Hu, H. W. Luyang, R. L. He, Z. J. Guan, S. F. Yuan and Q. M. Wang, Face-centered cubic silver nanoclusters consolidated with tetradentate formamidinate ligands, *J. Am. Chem. Soc.*, 2022, **144**, 19365–19371.

26 S. F. Yuan, C. Q. Xu, W. D. Liu, J. X. Zhang, J. Li and Q. M. Wang, Rod-shaped silver supercluster unveiling strong electron coupling between substituent icosahedral units, *J. Am. Chem. Soc.*, 2021, **143**, 12261–12267.

27 K. G. Liu, X. M. Gao, T. Liu, M. L. Hu and D. Jiang, All-carboxylate-protected superatomic silver nanocluster with an unprecedented rhombohedral Ag_8 core, *J. Am. Chem. Soc.*, 2020, **142**, 16905–16909.

28 S. F. Yuan, Z. J. Guan, W. D. Liu and Q. M. Wang, Solvent-triggered reversible interconversion of all-nitrogen-donor-protected silver nanoclusters and their responsive optical properties, *Nat. Commun.*, 2019, **10**, 4032.

29 C. Zhang, Y. M. Su, L. Li, Z. Wang, L. Feng, C. H. Tung and D. Sun, Supramolecular confinement of cyclodextrin-like host–guest polyoxovanadate in giant $Ag^{0/I}$ nanoclusters, *Angew. Chem., Int. Ed.*, 2025, **64**, e202506626.

30 Z. Wang, L. Li, L. Feng, Z. Y. Gao, C. H. Tung, L. S. Zheng and D. Sun, Solvent-controlled condensation of $[Mo_2O_5(PTC4A)_2]^{6-}$ metalloligand in stepwise assembly of hexagonal and rectangular Ag_{18} nanoclusters, *Angew. Chem., Int. Ed.*, 2022, **61**, e202200823.

31 X. M. Luo, C. H. Gong, X. Y. Dong, L. Zhang and S. Q. Zang, Evolution of all-carboxylate-protected superatomic Ag clusters confined in Ti-organic cages, *Nano Res.*, 2020, **14**, 2309–2313.

32 G. G. Luo, Q. L. Guo, Z. Wang, C. F. Sun, J. Q. Lin and D. Sun, New protective ligands for atomically precise silver nanoclusters, *Dalton Trans.*, 2020, **49**, 5406–5415.

33 M. Y. Gao, K. Wang, Y. Sun, D. Li, B. Q. Song, Y. H. Andaloussi, M. J. Zaworotko, J. Zhang and L. Zhang, Tetrahedral geometry induction of stable Ag–Ti nanoclusters by flexible trifurcate TiL_3 metalloligand, *J. Am. Chem. Soc.*, 2020, **142**, 12784–12790.

34 Z. Wang, Y. J. Zhu, B. L. Han, Y. Z. Li, C. H. Tung and D. Sun, A route to metalloligands consolidated silver nanoclusters by grafting thiacalix[4]arene onto polyoxovanadates, *Nat. Commun.*, 2023, **14**, 5295.

35 S. Yoo, D. Kim, G. Deng, Y. Chen, K. Lee, S. Yoo, X. Liu, Q. Tang, Y. J. Hwang, T. Hyeon and M. S. Bootharaju, Impact of heterocore atoms on CO_2 electroreduction in atomically precise silver nanoclusters, *J. Am. Chem. Soc.*, 2025, **147**, 12546–12554.

36 Y. Yao, W. Hao, J. Tang, K. Kirschbaum, C. G. Gianopoulos, A. Ren, L. Ma, L. Zheng, H. Li and Q. Li, Anomalous structural transformation of Cu(I) clusters into multifunctional CuAg nanoclusters, *Angew. Chem., Int. Ed.*, 2024, **63**, e202407214.

37 W. Q. Shi, L. Zeng, R. L. He, X. S. Han, Z. J. Guan, M. Zhou and Q. M. Wang, Near-unity NIR phosphorescent quantum yield from a room-temperature solvated metal nanocluster, *Science*, 2024, **383**, 326–330.

38 Y. Zeng, S. Havenridge, M. Gharib, A. Baksi, K. L. D. M. Weerawardene, A. R. Ziefuß, C. Strelow, C. Rehbock, A. Mews, S. Barcikowski, M. M. Kappes, W. J. Parak, C. M. Aikens and I. Chakraborty, Impact of ligands on structural and optical properties of Ag_{29} nanoclusters, *J. Am. Chem. Soc.*, 2021, **143**, 9405–9414.

39 K. Zheng, V. Fung, X. Yuan, D. Jiang and J. Xie, Real time monitoring of the dynamic intracluster diffusion of single gold atoms into silver nanoclusters, *J. Am. Chem. Soc.*, 2019, **141**, 18977–18983.

40 X. Kang and M. Zhu, Transformation of atomically precise nanoclusters by ligand-exchange, *Chem. Mater.*, 2019, **31**, 9939–9969.

41 X. Kang, L. Huang, W. Liu, L. Xiong, Y. Pei, Z. Sun, S. Wang, S. Wei and M. Zhu, Reversible nanocluster structure transformation between face-centered cubic and icosahedral isomers, *Chem. Sci.*, 2019, **10**, 8685–8693.

42 Y. Wang, H. Su, C. Xu, G. Li, L. Gell, S. Lin, Z. Tang, H. Häkkinen and N. Zheng, An intermetallic $Au_{24}Ag_{20}$ superatom nanocluster stabilized by labile ligands, *J. Am. Chem. Soc.*, 2015, **137**, 4324–4327.

43 Z. Wang, H. T. Sun, M. Kurmoo, Q. Y. Liu, G. L. Zhuang, Q. Q. Zhao, X. P. Wang, C. H. Tung and D. Sun, Carboxylic acid stimulated silver shell isomerism in a triple core–shell Ag_{84} nanocluster, *Chem. Sci.*, 2019, **10**, 4862–4867.

44 B. L. Lan, A. Y. Luo, B. Shao, L. N. Gao, Q. Wei, Y. N. Liang, J. Huang and Z. Zhang, Structural evolution from preorganized mononuclear triazamacrocyclic metalloligands to polynuclear metallocages and heterometallic 2D layers: modular architectures, assembly tracking and magnetic properties, *Dalton Trans.*, 2022, **51**, 16158–16169.

45 M. Y. Sun, L. Zhang, Y. Li, C. C. Wang, P. Wang, X. Ren and X. H. Yi, Recovering Ag^+ with nano-MOF-303 to form Ag/AgCl/MOF-303 photocatalyst: The role of stored Cl^- ions, *Chinese Chem. Lett.*, 2025, **36**, 110035.

46 M. Kamachi, K. Yonesato, T. Okazaki, D. Yanai, S. Kikkawa, S. Yamazoe, R. Ishikawa, N. Shibata, Y. Ikuhara, K. Yamaguchi and K. Suzuki, Synthesis of a gold–silver alloy nanocluster within a ring-shaped polyoxometalate and its photocatalytic property, *Angew. Chem., Int. Ed.*, 2024, **63**, e202408358.

47 M. Walter, J. Akola, O. Lopez-Acevedo, P. D Jadzinsky, G. Calero, C. J. Ackerson, R. L. Whetten, H. Grönbeck and H. Häkkinen, A unified view of ligand-protected gold clusters as superatom complexes, *P. Natl. Acad. Sci. USA*, 2008, **105**, 9157–9162.

48 N. Kitjanukit, W. Neamsung, A. Karawek, N. Lertthanaphol, N. Chongkol, K. Hiramatsu, T. Sekiguchi, S. Pornsuwan, T. Sakurai, W. Jonglertjunya, P. Phadungbut, Y. Ichihashi and S. Srinives, Effects of alcohols as sacrificial reagents on a copper-doped sodium dititanate nanosheets/graphene oxide photocatalyst in CO_2 photoreduction, *RSC Adv.*, 2024, **14**, 27980–27989.

49 A. Roucoux, J. Schulz and H. Patin, Reduced transition metal colloids: A novel family of reusable catalysts?, *Chem. Rev.*, 2002, **102**, 3757–3778.

50 N. Zhang, F. Qu, H. Q. Luo and N. B. Li, Sensitive and selective detection of biothiols based on target-induced agglomeration of silvernanoclusters, *Biosens. Bioelectron.*, 2013, **42**, 214–218.

51 Y. Zhang, M. Yang, Z. Shao, H. Xu, Y. Chen, Y. Yang, W. Xu and X. Liao, A paper-based fluorescent test for determination and visualization of cysteine and glutathione by using gold-silver nanoclusters, *Microchem. J.*, 2020, **158**, 105327.

52 X. Lin, Z. Hao, H. Wu, M. Zhao, X. Gao, S. Wang and Y. Liu, A ratiometric fluorescent nanoprobe consisting of ssDNA-templated silver nanoclusters for detection of histidine/

cysteine, and the construction of combinatorial logic circuits, *Microchim. Acta*, 2019, **186**, 648.

53 B. Zhang, L. Chen, M. Zhang, C. Deng and X. Yang, A gold-silver bimetallic nanocluster-based fluorescent probe for cysteine detection in milk and apple, *Spectrochim. Acta A*, 2022, **278**, 121345.

54 X. Fang, H. Sun, C. Wu, Z. Fang, M. Li, L. Zhao, B. Tian, P. Verma, J. Wang, R. Maeda and Z. Jiang, Ag nanoparticle-thiolated chitosan composite coating reinforced by Ag–S covalent bonds with excellent electromagnetic interference shielding and joule heating performances, *ACS Appl. Mater. Interfaces*, 2023, **15**, 28465–28475.

55 X. L. Li, S. Huang, D. Yan, J. Zhang, D. Fang, Y. V. Lim, Y. Wang, T. C. Li, Y. Li, L. Guo and H. Y. Yang, Tuning lithiophilicity and stability of 3D conductive scaffold via covalent Ag–S bond for high-performance lithium metal anode, *Energy Environ. Mater.*, 2023, **6**, e12274.

56 X. Yuan, Y. Tay, X. Dou, Z. Luo, D. T. Leong and J. Xie, Glutathione-protected silver nanoclusters as cysteine-selective fluorometric and colorimetric probe, *Anal. Chem.*, 2013, **85**, 1913–1919.

57 J. Du, F. Jin, G. Jiang and Z. Jin, Synergistically regulating d-band centers of $Cd_{0.5}Zn_{0.5}S/LaCoO_3$ heterojunction by dual electric fields for enhanced photocatalytic hydrogen evolution, *Chem. Mater.*, 2025, **37**, 2664–2675.

58 C. Huang, X. Zhang, D. Li, M. Wang and Q. Wu, The influence of the precursor molar ratio on the structure of the CdS catalyst during synthesis and visible-light driven CO_2 reduction into solar fuel, *New J. Chem.*, 2022, **46**, 10339–10346.

59 Y. Wang, X. Xu, W. Lu, Y. Huo and L. Bian, A sulfur vacancy rich CdS based composite photocatalyst with g-C_3N_4 as a matrix derived from a Cd–S cluster assembled supramolecular network for H_2 production and VOC removal, *Dalton Trans.*, 2018, **47**, 4219–4227.

60 D. I. Krisnawati, P. H. Hsu, Y. H. Lin, M. Alimansur, D. S. Atmojo, E. Q. Rahmawati, D. Rahayu, M. Khafid, S. C. Lu and T. R. Kuo, The use of the ROS scavenger cysteine as a surface ligand of metal nanoclusters and its bactericidal elimination effect, *Appl. Sci.*, 2021, **11**, 4095.

61 T. Kurihara, Y. Noda and K. Takegoshi, Capping structure of ligand–cysteine on CdSe magic-sized clusters, *ACS Omega*, 2019, **4**, 3476–3483.

62 H. Huang, H. Li, J. J. Feng, H. Feng, A. J. Wang and Z. Qian, One-pot green synthesis of highly fluorescent glutathione-stabilized copper nanoclusters for Fe^{3+} sensing, *Sensors Actuat. B-Chem.*, 2017, **241**, 292–297.

63 (*a*) CCDC 2464348: Experimental Crystal Structure Determination, 2025, DOI: **10.5517/ccdc.csd.cc2nqc3w**; (*b*) CCDC 2464349: Experimental Crystal Structure Determination, 2025, DOI: **10.5517/ccdc.csd.cc2nqc4x**; (*c*) CCDC 2464350: Experimental Crystal Structure Determination, 2025, DOI: **10.5517/ccdc.csd.cc2nqc5y**; (*d*) CCDC 2464351: Experimental Crystal Structure Determination, 2025, DOI: **10.5517/ccdc.csd.cc2nqc6z.**